

Plasticity and damage in cellular amorphous metals

A.H. Brothers, D.C. Dunand *

Department of Materials Science and Engineering, Northwestern University, Cook Hall, 2220 Campus Drive, Evanston, IL 60208 3108, USA

Received 8 April 2005; received in revised form 2 June 2005; accepted 2 June 2005

Available online 2 August 2005

Abstract

Compressive mechanical properties of low-density, open-cell Zr-based bulk metallic glass foams processed by the salt replication method are investigated as a function of relative density and pore size in the ranges 14–28% and 150–355 μm , respectively. Scaling behaviors for strength and stiffness are discussed in the context of models developed for conventional metal foams, and appropriate modifications presented where necessary. Deformation and damage features not addressed by such models are then discussed in terms of the unique conditions allowing ductility in amorphous metal foams. It is shown that despite a small number of brittle uniaxial strut failures, ductile deformation by strut bending predominates in the foams, with the result that all but the densest foam could be compressed to a nominal strain in the vicinity of 80% without macroscopic fracture.

© 2005 Acta Materialia Inc. Published by Elsevier Ltd. All rights reserved.

Keywords: Metallic glasses; Foams; Vit106; Mechanical properties; Shear bands

1. Introduction

Amorphous metals offer unique potential as structural materials, having high strength, hardness, wear and corrosion resistance alongside modest processing temperatures and densities [1,2]. Unfortunately, these properties cannot be fully exploited in monolithic amorphous metals due to their lack of plasticity in unconfined loading geometries (the sole exception being one intrinsically ductile Pt-based alloy [3]). However, it was shown recently that substantial compressive plasticity can occur in porous metallic glasses with relatively high density and closed porosity, which were characterized by improved but still modest ductility (<16% failure strain) [4]. Still higher compressive ductility (>50% failure strain) was measured in a low-density Zr-based amorphous metal foam with open-cell architecture, which exhibited compressive properties qualitatively similar

to foams made from ductile crystalline metals such as aluminum [5]. This very high ductility arose from the formation of stable shear bands within the slender struts that typically comprise low-density, open-cell foams [6,7]. Its effective use should allow amorphous metal foams to compete with conventional crystalline metal foams in advanced multifunctional applications such as lightweight structures, energy absorbers, or biomaterials [8].

Though amorphous metal foams have now been processed by several methods using both Pd- and Zr-based alloys [4,5,9–13], and though mechanical properties have been reported [4] for a series of relatively high-density, closed-porosity metallic glasses, no data series exists for low-density, open-cell foam architectures, whose properties more closely resemble those of conventional cellular materials and whose structures are most suited to the conditions of stable shear banding [5]. Here, we provide such data for cellular metallic glasses made from a commercial alloy by the salt replication method, where we systematically vary pore size and density. Results are interpreted within the context of models developed for conventional metallic foams, with adaptations taking

* Corresponding author. Tel.: +1 847 491 5370; fax: +1 847 491 7820.

E-mail addresses: a-brothers@northwestern.edu (A.H. Brothers), dunand@northwestern.edu (D.C. Dunand).

into account particular mechanical features of amorphous metals where necessary. Also, unique aspects of their mechanical behavior are discussed in terms of the coexistence of brittle and ductile strut deformation modes, and this is correlated to the evolution of damage inside the foams.

2. Materials and methods

Amorphous metal foams were prepared by the salt replication method, reported in detail elsewhere [13] and summarized as follows. Monocrystalline BaF_2 powders (99.999%) were graded using sieves into 150–212, 212–250, and 300–355 μm ranges and vacuum-sintered (10 h, 1250 °C) into 6 mm diameter porous cylindrical patterns. Amorphous Vit106 (Zr–5 at.%Nb–15.4 at.%Cu–12.6 at.%Ni–10 at.%Al), which was produced by arc melting of high-purity ($\geq 99.5\%$) metals, was remelted under high vacuum (<4 mPa) in stainless-steel crucibles and pressure-infiltrated (975 °C, 55 kPa gauge pressure of high-purity Ar) into the BaF_2 patterns. After water-quenching, the Vit106/ BaF_2 composites were machined into uniform cylinders with diameters of 3.5–4.5 mm (mean: 4.0 mm) and aspect ratios of 1.5–2.2 (mean: 1.9) using a diamond grinding wheel and a diamond wafering saw. To eliminate size effects, the diameter of each sample was at least one order of magnitude greater than the maximum salt particle size of its pattern [14]. For comparison purposes, a pure (99.99%) aluminum foam of 28% relative density was also made by infiltration (750 °C, 3.4 kPa Ar gauge pressure) of unsintered NaCl (pore size ~ 500 μm) followed by dissolution of the salt in water. A compression specimen with diameter 3.8 mm and aspect ratio 2.0 was produced from this aluminum foam by wire electric discharge machining.

After machining, the Vit106 phase of each composite was tested for crystallinity by Cu $K\alpha$ X-ray diffraction (XRD) performed on cross-sections far from all surfaces nearest the quench bath; only fully amorphous samples are described here. Following XRD analysis, BaF_2 patterns were dissolved by suspension in ultrasonically agitated 2M HNO_3 baths equilibrated to 50–55 °C and refreshed periodically to avoid buildup of corrosive fluoride ion. Suspension was continued until each sample reached a target relative density, as determined from dry mass and sample dimensions. Minimum relative density (ca. 15%) was limited by the density at which foams became fragile and prone to surface irregularity and damage during handling; maximum density (ca. 28%) was limited by the need to assure near-complete removal of BaF_2 patterns. At this maximum density, a few isolated BaF_2 deposits were visible at the center of the sample following compression testing. No such deposits were found in foams of lower relative density. Though final pore sizes were slightly higher than the nominal salt

grades due to the corrosive action of the acid baths required to leach the salt, these changes were small, and thus for brevity the approximate midrange values (180, 230, and 330 μm) are used here to denote pore sizes.

Secondary-electron scanning electron microscopy (SEM) was performed using a Hitachi-3500S. Where necessary, samples were sputter-coated with 15–20 nm of Au/Pd prior to SEM imaging. Compressive properties of Vit106 foams were measured during displacement-controlled uniaxial compression at nominal strain rates of $5 \times 10^{-4} \text{ s}^{-1}$ using a screw-driven load frame with oil-lubricated carbide platen inserts and a cage ensuring parallelism. Load train compliance corrections were made for every sample using data measured prior to and after each test, and data are presented throughout as engineering stress and strain. Reloading stiffness was calculated from reload branches during periodic unload/reload cycles. To avoid sample resettling during these cycles, only 50% of the flow stress was unloaded, and points near reversal of the cross-head motion were discarded. The aluminum foam specimen was compressed at a nominal strain rate of $2 \times 10^{-4} \text{ s}^{-1}$ without carbide inserts and using a laser extensometer, to improve strain resolution in light of its lower strength. Errors and error bars, including errors for stiffness calculated by linear least-squares regression, represent 95% confidence intervals assuming independent randomly distributed errors having zero mean and constant variance [15].

3. Results

3.1. Structure

Scanning electron micrographs showing the size and shape of unsintered and as-sintered 230 μm BaF_2 particles are shown in Fig. 1(a) and (b), respectively. Unsintered BaF_2 particles were elongated and angular; though sharp particle edges showed some rounding, sintering did not substantially alter either aspect ratio or overall angularity, and faceting of the particles was not observed. Analysis of visible necks within the sintered pattern indicated neck widths primarily in the range of 20–60 μm . After infiltration of sintered patterns (Fig. 1(c)) with molten Vit106, no significant porosity was observed using optical microscopy, suggesting that replication of the topological features of the salt was complete. As expected, the resulting foam structures contained angular pores, and some elongated pores (though due to the randomness of particle packing, this was not expected to lead to macroscopic anisotropy), as illustrated in Fig. 1(d) and (e). No clear evidence was found that this angularity was mitigated through the leaching process, despite the expectation that highly convex surfaces, such as sharp edges and

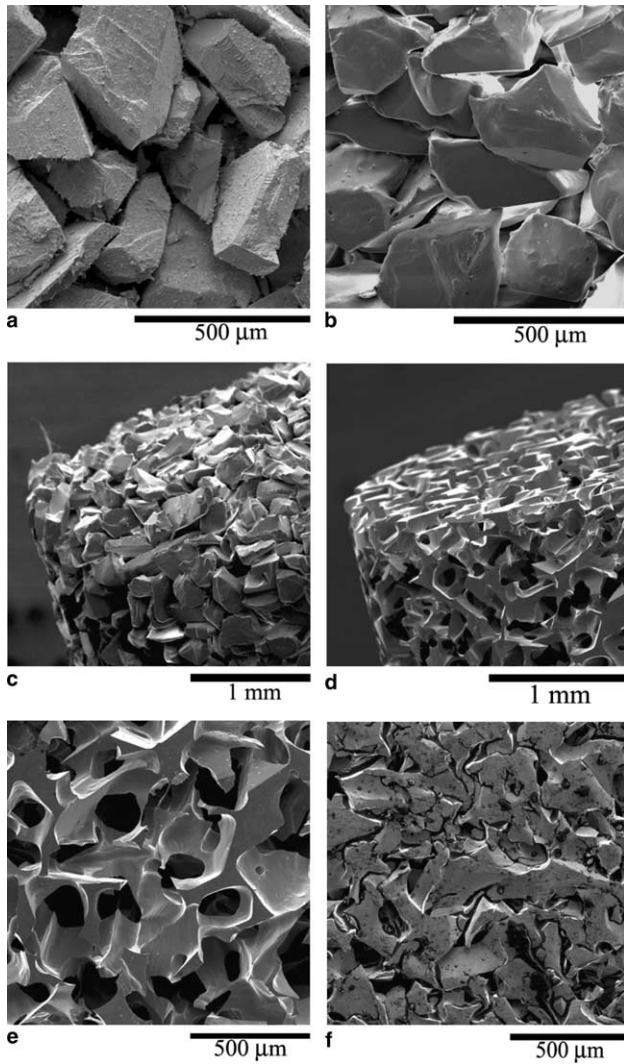


Fig. 1. SEM micrographs showing: (a) morphology of unsintered 230 μm BaF₂ powders; (b) morphology of as-sintered 230 μm BaF₂ powders, showing slight rounding but no substantial reshaping; (c) macrostructure of a sintered 230 μm BaF₂ pattern before infiltration; (d) macrostructure of Vit106 foam (22% dense) replicated from a 230 μm pattern; (e) magnified view of the foam in panel (d), showing pore, strut and node structure; (f) view of the deformed foam in panels (d,e) after unloading from 79% engineering strain.

corners, should be more susceptible to corrosion. After compression to high (ca. 80%) strain, the foam structure was uniform and visibly dense, with the exception of the sample edges; no sign of macroscopic sample cracking was visible after unloading (Fig. 1(f)).

A series of SEM images depicting the deformation of a sample of pore size 230 μm and relative density 23%, after unloading at regular intervals up to a strain of 43%, is shown in Fig. 2(a)–(c). Except for some minor shearing (Fig. 2(b) and (c)), deformation was uniform to the naked eye with no evidence of ‘crush bands’ often reported in other foam materials [14,16]. Though the comparatively high density of this sample and the existence of large nodes connecting struts, prevented line

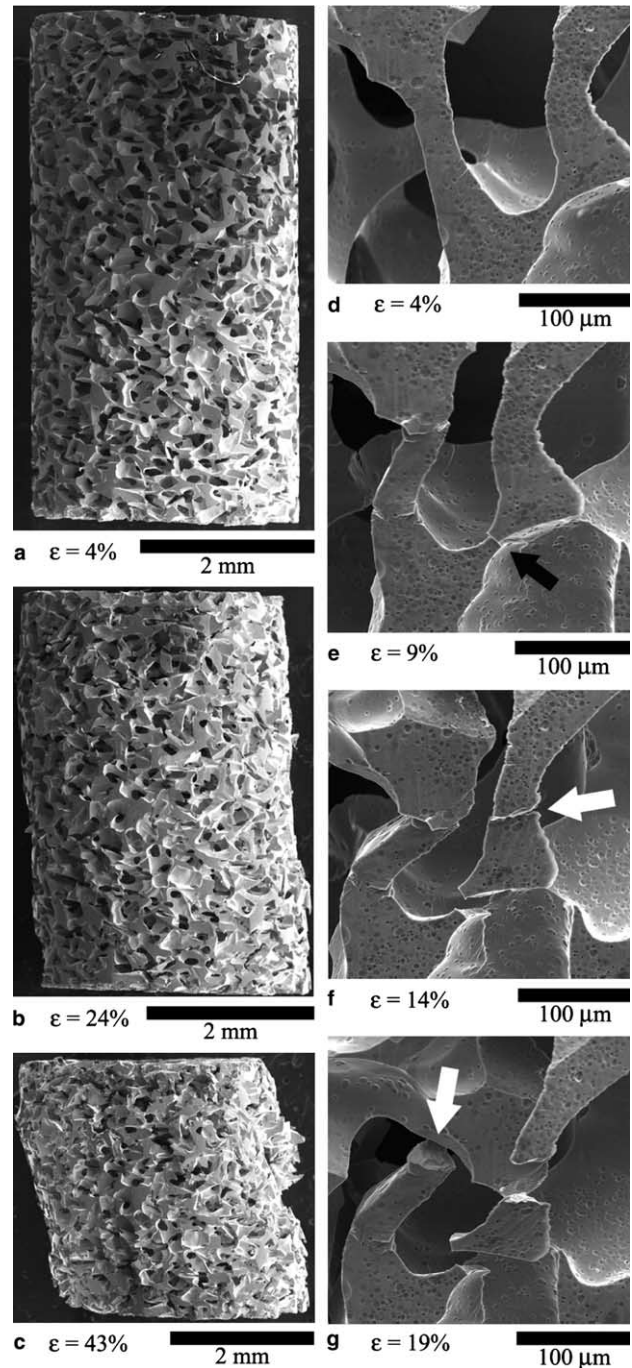


Fig. 2. SEM micrographs illustrating mechanisms of compressive deformation in Vit106 foams (pore size 230 μm and relative density 23%, similar to the foam in Fig. 1(d) and (e)). Low-magnification images show foam structure following unloading from various applied macroscopic strains: (a) low strain (4%); (b) intermediate strain (24%); (c) high strain (43%). Also shown are deformed struts within the sample following unloading from: (d) 4% strain; (e) 9% strain; (f) 14% strain; (g) 19% strain. Visible fractures are indicated by arrows in the panels where they first appear.

of sight through the sample and may have obscured any visible evidence, it is notable that uniform deformation was also reported in comparable Al-based foams

made using NaCl [17]. Images illustrating local deformation in a pair of adjacent slender struts near the surface of this sample are shown in Fig. 2(d)–(g). One of these struts (left in Fig. 2(d)–(g)) underwent pronounced plastic deformation near its junctions with adjoining nodes (i.e., plastic hinging) before fracturing when the foam reached an average uniaxial strain between 14% and 19%. By contrast, the neighboring strut (right in Fig. 2(d)–(g)) showed little or no visible plasticity, succumbing to fracture at lower applied strain (one crack appeared between 4% and 9% strain, a second between 9% and 14%). Many further instances of both deformation modes were observed, indicating that both occurred frequently and were distributed with high uniformity inside the foam.

3.2. Compressive mechanical properties

Engineering compressive stress–strain curves are shown as a function of density for samples of constant pore size (230 μm) in Fig. 3(a), and as a function of pore size for samples of near-constant relative density (22.4–23.8%) in Fig. 3(b). The densest sample examined (28%) exhibited ductile foam behavior up to ca. 50% strain, at which point a portion of the densified foam fractured from the sample, and the test was terminated. Though minor ‘spalling’ of material was apparent from the side surfaces of all Vit106 samples at high strain, the remaining samples were compressed to strains in the vicinity of 80% without macroscopic fracture, and exhibited behavior typical of ductile metallic foam in compression: an initial linear, pre-yield region followed by a second post-yield region of slowly rising flow stress. Denser samples showed smaller relative increases in flow stress after yield (about 3-fold by 50% strain, compared to more than 6-fold for the least-dense sample over the same interval). No dependence on pore size, other than variations in the intensity of serrations (discussed in detail in Section 4.6), was observed up to a strain of 25%; thereafter, a somewhat faster increase in flow stress was recorded as the pore size decreased, Fig. 3(b). The relative increase in flow stress following yield in the aluminum foam was approximately 10-fold over the same range of strain, significantly higher than in any Vit106 sample.

In each sample, abrupt losses in flow stress occurred throughout the post-yield linear region of the stress–strain curve (Fig. 3, insets), where they were visible as serrations followed by gradual recoveries. These serrations were accompanied by emission of sparks from the foam interiors, and sparks were also observed during uniaxial failure of large monolithic Zr-based amorphous metals. Such emissions can be attributed to high elastic energy release (due to high strength and low modulus [18]) combined with the exothermic oxidation of Zr-based particulates expelled during fracture. All curves

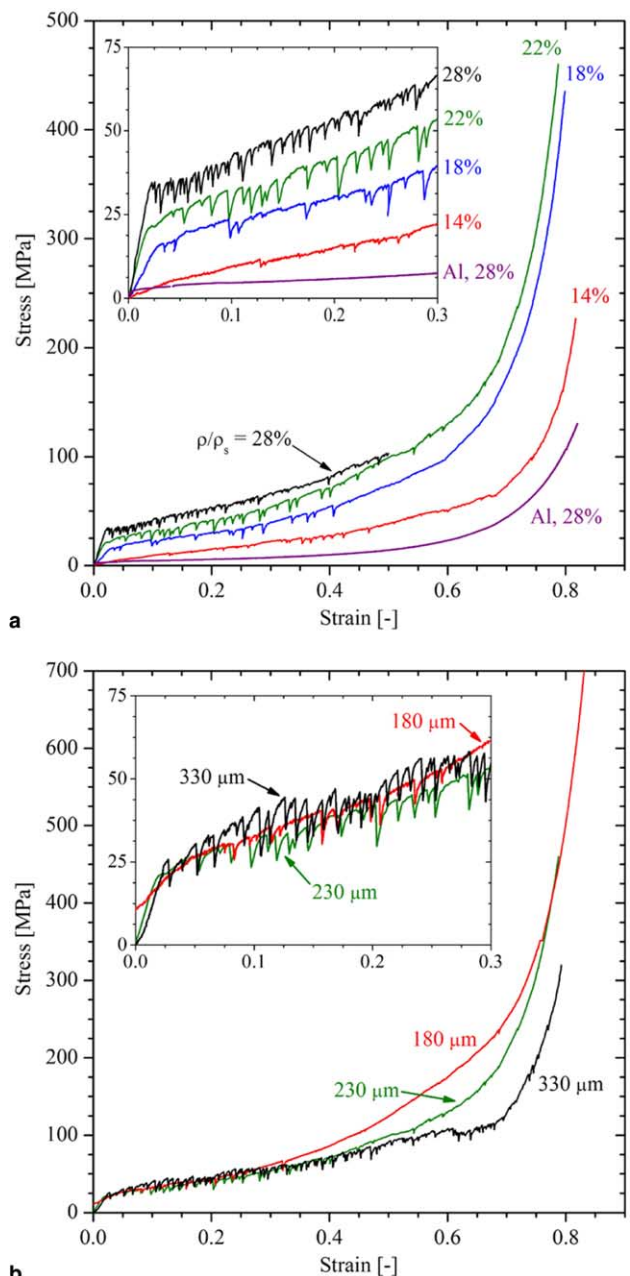


Fig. 3. Engineering compressive stress–strain curves of Vit106 foams (a) as a function of relative density for constant pore size 230 μm ; and (b) as a function of pore size for near-constant relative density (22.4–23.8%). Insets magnify the low-strain regions for better visualization of serrations.

(except for the foam that fractured) were also terminated at high strains by rapidly increasing flow stress (i.e., densification). Final densification was gradual, as for all ductile foams, and difficult to identify exactly due to the gradually changing slopes of the stress–strain curves [14,17]. Thus densification strains were assigned systematically using the intersection of two lines, the first drawn along the post-yield linear region between 10% and 30% strain and the other tangent to the stress–strain curve at a strain of 70%, which visibly

exceeded the onset of densification in all samples. Densification strains using this method ranged from 60% to 66%; for the purposes of strain energy calculations, densification strain for the prematurely fractured sample (28% relative density) was taken to be 50%. Using this same method, the densification strain of the aluminum foam was 61%, within the range of the Vit106 foams.

The necessary use of aggressive leaching media in removing the BaF_2 placeholders implied that relative density decreases were largely affected through corrosive attack of the alloy, a process proceeding more rapidly on high-surface-area features like struts and less rapidly on the nodes connecting the struts [13]. The effect of this non-uniform mass loss was most pronounced at the lowest relative densities (14–15%), where foam surface damage was visible in the form of uneven sample surfaces, preventing full contact with the compression platens at low strains. As a result, this sample showed (Fig. 3(a), inset) an unrealistically high yield strain ca. 4% and proportionally erroneous stiffness, as a result of early yield representing only the contacted portion of the sample. This sample was included for completeness, and also because its high-strain properties (e.g., those related to serrations and densification) were still believed valid; however, its low-strain data, assumed to contain contributions from damage and surface unevenness, were not included in analysis involving stiffness or strength. The onset of such deterioration at non-zero relative density confirmed the existence of mass localization at nodes, which contribute little to mechanical properties at low strains. Additionally, the sample of relative density 24% and 180 μm pore size was used to investigate the possibility of acoustic emissions measurements, the results of which will be discussed elsewhere. For present purposes, it is noted that the use of silicone coupling fluid on the sample faces during compression led to a similar result (Fig. 3(b), inset) as for the low-density sample above, reducing accuracy of the lowest-strain data. It is believed that the yield stress of this sample was accurate but, due to the layer of coupling fluid, the loading stiffness and yield strain were inaccurate, being too low and too high, respectively.

The Vit106 foam stiffness as measured during initial loading increased with relative density, as shown in Fig. 4(a) for all samples. Generally, stiffness data taken from reloading following unloading just below the yield stress are preferred over those from initial loading, on account of sample misalignment and strut microplasticity and/or reorientation during initial loading, leading to low apparent loading stiffness [14]. Stiffness was nevertheless measured from initial loading, employing the full extent of the initial linear regions, to avoid the larger error associated with the reload data, for which less than half the linear stress–strain region could be used due to sample resettling (Section 2). Reload stiffness data were, however, reliable for certain

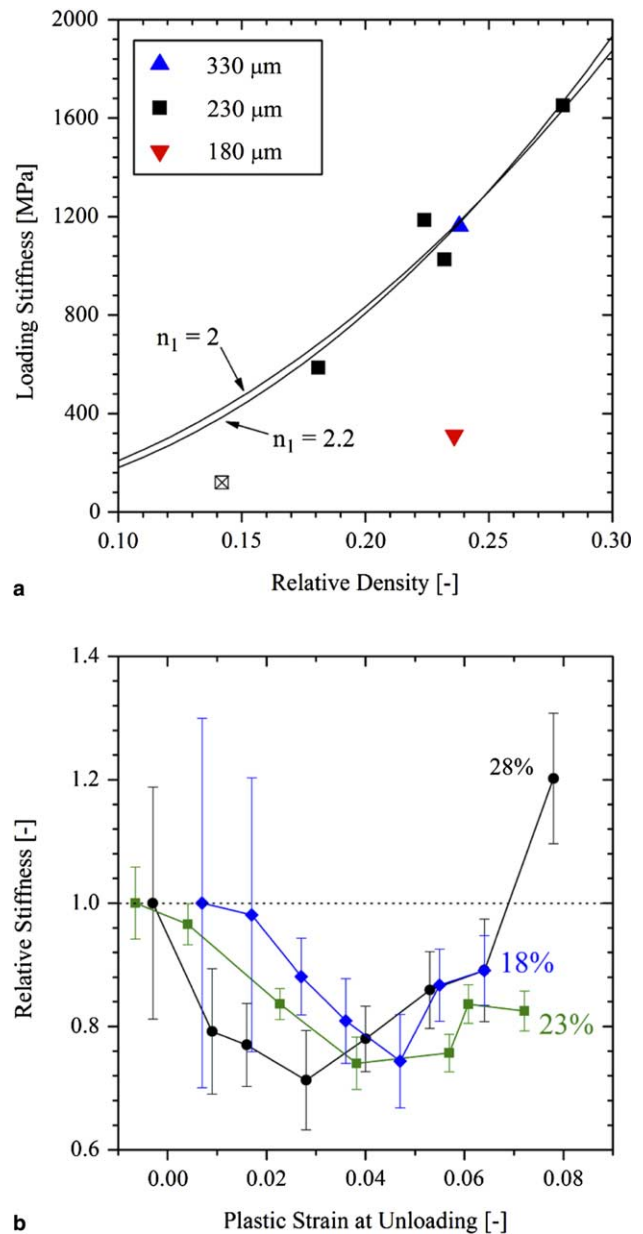


Fig. 4. Stiffness of Vit106 foams. (a) Initial loading stiffness for all samples, as a function of relative density and pore size. Also shown are best fits according to a power-law scaling relationship, Eq. (1), using $(C_1, n_1) = (0.30, 2.2)$ and $(0.24, 2)$. The point representing the damaged 14% sample was not used in regression and is denoted by an open symbol. (b) Reload stiffness for a foam with 230 μm pore size and 28% relative density as a function of plastic strain. Data were normalized by the stiffness immediately prior to yield (1.9% strain). Also shown for completeness are similar data from other foams of equal pore size but varying density, showing less precision but similar overall behavior.

samples having higher yield stresses or longer gauge lengths, as determined using the calculated error bars. Reload stiffness was measured for these samples as a function of strain and is shown in Fig. 4(b) after normalization by initial stiffness, i.e. by the stiffness measured closest to yield. Reload stiffness for the

densest sample (28%) immediately prior to yield (nominal strain 1.9%, with estimated yield at 2.0%) was 2.8 GPa, ca. 70% greater than initial loading stiffness, such increases being also observed in other metallic foams [14]. Stiffness in this sample initially decreased with increasing plastic strain, reaching after a strain of ca. 5% a minimum of about 70% of its value at yield. Thereafter the sample stiffness increased, surpassing its initial value at a strain of about 9–10%. Though other samples showed high scatter, as stated previously and as shown in Fig. 4(b), similar trends were observed, with stiffness achieving a minimum in the range of 5–7% strain.

Compressive yield strength was defined by the intercept of tangents in the immediate pre- and post-yield portions of the stress–strain curve; the existence of pronounced serrations post-yield, and the resulting difficulty in accurately defining a tangent there, introduced some error into yield stress values. Within this uncertainty, no difference was detected between the strength (or indeed between the whole stress–strain curves) of two foams of 230 μm pore size and similar relative densities (23.2% and 22.4%), but with different diameters (3.0 and 4.5 mm, respectively). Because all other sample diameters lay between these limits, it was concluded that sample size effects were not appreciable within the samples tested. It is further noted that no significant change in strength was observed as a function of pore size for samples of similar relative density (23.2–23.8%), as shown in Fig. 3(b). The early portions of the stress–strain curves (Fig. 3(a), inset), however, clearly show

that yield strength increased with density, with values ranging between about 6 and 34 MPa (here, we employ the term ‘yield stress’ rather than ‘plateau stress’, since flow stresses rose substantially between yielding and final densification). Yield stress data for all samples are shown in Fig. 5 as a function of relative density and pore size.

4. Discussion

4.1. Processing and structure

The processing and structure of metallic foams made by salt replication methods have been discussed elsewhere for crystalline metals [19,20], and for amorphous metals [5,8,13], for which additional requirements include high cooling rates and compositional accuracy (thus dictating the choice of highly stable salts). From the standpoint of mechanical properties, there appear to be three salient features to replicated metallic foams. Firstly, salt replication allows small and tightly distributed pore sizes which, in turn, allow statistically reliable property measurements in smaller samples; this is particularly important for amorphous metal foams due to the sample size limitations imposed by the vitrification requirement [8]. Secondly, pore morphologies in replicated foams faithfully reflect salt powder morphologies, and control over salt morphology has already been used to modify the pore structure of aluminum foams made with NaCl [21]. Less flexibility exists with low-solubility, slow-sintering patterns like BaF₂, whose angular morphology (Fig. 1(a)) does not appear to be mitigated significantly during sintering (Fig. 1(b)) and which persists in the replicated alloy structure even after corrosion processes (Fig. 1(e)). Angular pores induce high stress concentrations in the foam and are therefore less desirable than rounded pores; pore morphology is known to affect the strength of ductile aluminum foams [22], and amorphous metal foam struts, especially those prone to brittle failure due to low aspect ratio or local loading conditions favoring axial deformation, may be particularly sensitive to stress concentrations. Indeed, angular pore morphology has already been invoked to explain observed strength losses in higher-density Pd-based amorphous metal foam [4,10]. Finally, the irregular packing of aspherical salt grains leads to inefficiency in mass distribution in the replicated foams, which do not perfectly resemble low-density open-cell foams made by other methods but show more pronounced localization of mass in the nodes (Fig. 1(e)) [19,20]. Similarly, because salt-replicated structures are not dictated by surface energy minimization like open-cell foams produced by most other melt-based methods, the shapes of struts and nodes tend to be irregular [14,20]. While some redistribution of mass towards the nodes (i.e., strut tapering) can improve

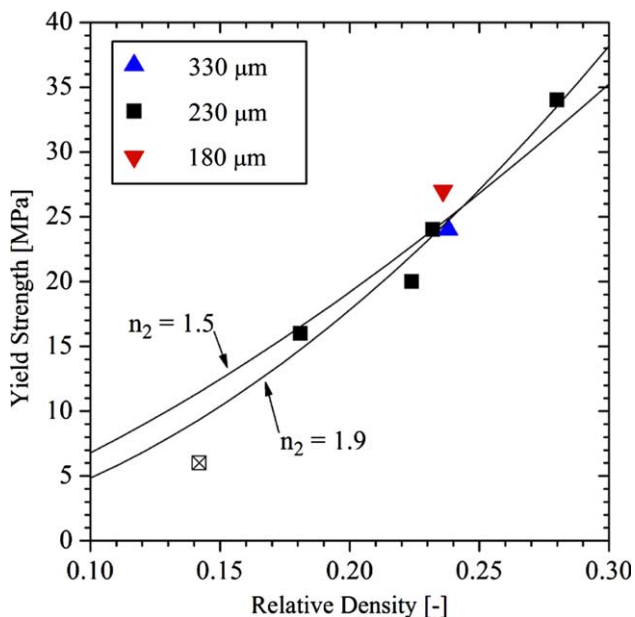


Fig. 5. Yield strength for Vit106 foams as a function of relative density and pore size. Also shown are best fits according to a power law scaling relationship, Eq. (2), using $(C_2, n_2) = (0.26, 1.9)$ and $(0.15, 1.5)$. The point representing the damaged 14% sample was not used in regression and is denoted by an open symbol.

mechanical properties by concentrating mass in portions of the strut subject to the highest bending moments [23], it may prove deleterious for amorphous metal foams, whose ductility depends on maximizing the mass fraction appearing as small, slender struts capable of bending deformation through stable shear banding processes.

4.2. Stiffness and strength

The stiffness E and strength σ_y of crystalline metallic foams are known, on the basis of dimensional arguments and empirical data, to exhibit power-law scaling behavior of the forms

$$\frac{E}{E_s} = C_1 \left(\frac{\rho}{\rho_s} \right)^{n_1}, \quad (1)$$

$$\frac{\sigma_y}{\sigma_{y,s}} = C_2 \left(\frac{\rho}{\rho_s} \right)^{n_2}, \quad (2)$$

where the subscripts y denote yield strength, subscripts s denote the properties of the solid phase, and C_1 , C_2 , n_1 , and n_2 are fitting parameters [14]. Least-squares regression of initial loading stiffness data from Vit106 foams of 230 μm pore size (Fig. 4(a); using $E_s = 86.7$ GPa [18]) provide $C_1 = 0.30$ and $n_1 = 2.2$, within the range of 1.8–2.2 found in crystalline metal foams but slightly above the most common value $n_1 = 2$. Although this may suggest a slightly more rapid stiffness loss with decreasing density, as might be expected given the non-uniform dissolution process underlying density decreases in Vit106 foam, use of the commonly accepted value for n_1 also gives an acceptable fit to the data, considering the limited number of data points. A similar analysis of strength data from foams of 230 μm pore size (Fig. 5) gave a scaling exponent of $n_2 = 1.9$, also within the empirical range of $n_2 = 1.5$ –2.0 for crystalline metal foams, and above the commonly accepted value of 1.5 [14]. Once again, use of the conventional scaling exponent gave an adequate fit to Vit106 data. Consequently, both stiffness and strength may be said to scale with relative density in approximately the same way for Vit106 as for crystalline metal foams, within the density range examined here (18–28%). Slightly more rapid loss in both stiffness and strength may have occurred in Vit106 foams, which would be in accordance with expectations related to their processing, but the difference was not significant. The best-fit curves for stiffness and strength are shown in Figs. 4(a) and 5, respectively, along with those representing ‘conventional’ behavior (i.e., $n_1 = 2$ and $n_2 = 1.5$).

Fig. 6(a) and (b) show normalized stiffness and strength data for Vit106 foams alongside data from higher-density, closed-cell porous Pd-based amorphous metal [4]. Bulk Young’s moduli were taken to be 86.7 GPa [18] for Vit106 and 102 GPa for $\text{Pd}_{42.5}\text{Cu}_{30}\text{Ni}_{7.5}\text{P}_{20}$ [4]. Bulk compressive strength was used to

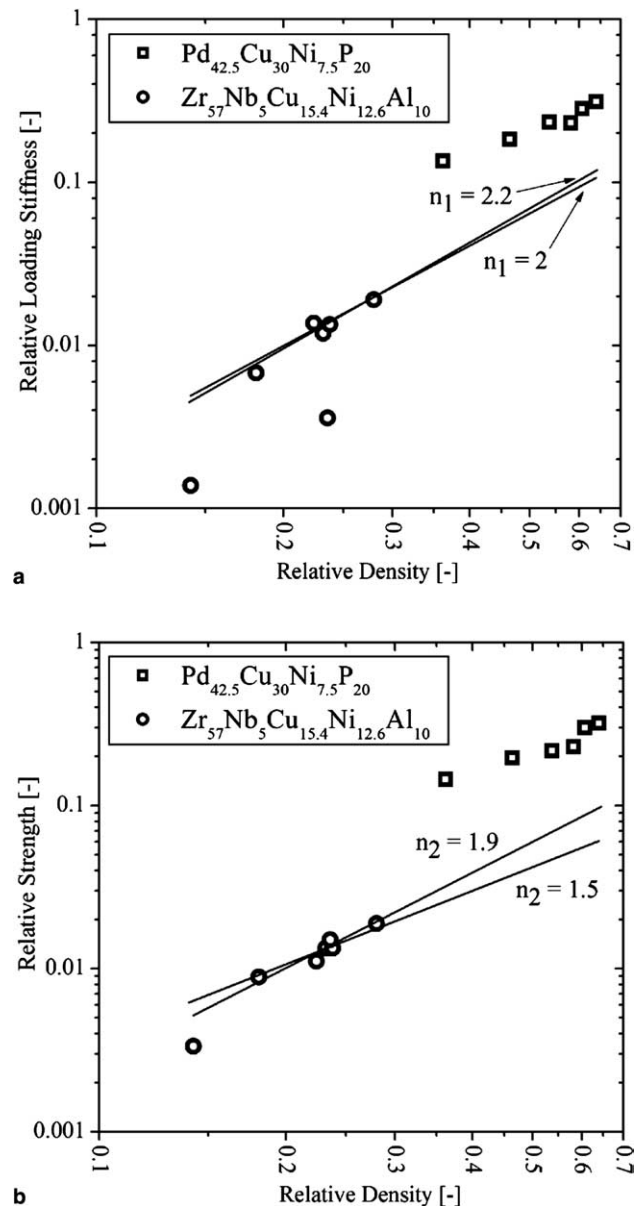


Fig. 6. Normalized loading stiffness (a) and compressive strength (b) for both low-density open-cell Vit106 foams (circular markers) and closed-cell porous Pd-based bulk metallic glasses (square markers, Ref. [4]) as functions of relative density.

normalize foam strengths (see Section 4.3); values were 1800 MPa for Vit106 [24] and 1650 MPa for $\text{Pd}_{42.5}\text{Cu}_{30}\text{Ni}_{7.5}\text{P}_{20}$ [4]. The two sets of data show, even on logarithmic scales, visible differences. Specifically, normalized stiffness and strength were higher for the high-density porous structures, even when the trend of the low-density foams is extended to higher densities. This is to be expected for several reasons: first, the Pd-based alloys had closed-cell structures, which tend to be somewhat stronger and stiffer than open-cell structures of equal density [14,25]. Second, with regard specifically to strength, the pores in the Pd-based structure were more rounded, minimizing loss in strength associated with

stress concentrations. The significance of these two effects is evident in the loss of stiffness and strength in NaCl-replicated Pd-based BMG foams having open, angular cells [10], as compared to closed-cell, spherical-pore foams of equal density [4]. Third, the higher-density Pd-based foams derived their ductility (failure strains around 16% or less, similar to many amorphous metal–matrix composites but much less than the present cellular amorphous foams) through shear band arrest rather than through stable shear band formation in struts, as indicated by examination of deformed specimens [4,5]. These porous structures failed locally through axial deformation of a matrix containing pores, rather than by bending of distinct struts as in low-density cellular structures. Since the load-bearing capacity of a metallic glass feature such as a strut is substantially higher in axial loading than in bending, loss in strength is expected to accompany the transition between axial and bending-dominated deformation modes, especially since collapse in bending is partly controlled by the tensile strength (1200 vs. 1800 MPa in compression for Vit106 [18]). A similar loss in stiffness may occur during the transition to bending-dominated deformation, since elastic deflection of a long beam subjected to bending, e.g. in a cantilever, is generally higher than the deflection of an identical beam deforming axially under the same load. This effect is less pronounced than for strength, due to the absence of tension–compression asymmetry in alloy stiffness. Though it is difficult to extract the contributions of the other factors given above, the discontinuity in strength and stiffness between the two data sets in Fig. 6(a) and (b), together with the pronounced change in ductility, suggests that such a transition may occur in the neighborhood of 30% relative density.

In the absence of processing-related microstructural variations, most data show no distinct variation of foam stiffness with pore size for either ductile [22] or brittle [26] foams; an increase in stiffness at low pore size, however, has been reported in Mg-based foams [27]. Due to the effect of acoustic coupling fluid on the 180 μm sample, it is not possible to verify here the presence or absence of a similar trend in Vit106; the two larger pore sizes (230 and 330 μm), however, did indeed show very similar loading stiffness. On the other hand, an inverse dependence of compressive strength on pore size has been reported for brittle ceramic foams, e.g., silicate glass [28] and glassy carbon [26], even in the absence of microstructural variations. This dependence may be rationalized using Weibull weakest-link approaches and arises from decreasing strut volume and surface area with decreasing pore size, and consequent increases in effective strut strength [26,28,29]. The absence of significant pore size dependence in Vit106 compressive strength supports the view that Vit106 foams more closely resemble ductile crystalline metal foams than brittle ceramic foams. It is notable, however, that size effects in

high-strain compressive flow stress [21] and tensile strength [30] have been reported in some replicated aluminum foams, perhaps associated with differences in the density of geometrically necessary dislocations and oxide scale thickness, and that a small effect was found in replicated magnesium foam [27]. More complete investigation of this conclusion would be possible using foams with finer porosity, but this was not pursued here due to processing difficulties associated with infiltrating and leaching finer salt particles.

The coefficients C_1 and C_2 in Eqs. (1) and (2) are related to strut geometry (e.g. cross-sectional shape and uniformity) and the concentration and severity of defects; as such, they are often treated as ‘knockdown’ factors representative of the overall mechanical efficiency of the foam architecture. Empirical data for conventional metal foams are best fit by the values $C_1 \sim 1$ and $C_2 \sim 0.3$ [14,25]. The lower best-fit value of $C_1 = 0.30$ found for Vit106 was in part due to the non-optimal mass distribution in the structure, but also reflects the fact that initial loading stiffness is typically markedly smaller than unloading/reloading stiffness [14]. Quantitative evaluation of this statement is impossible without full reloading stiffness data, but the high reloading stiffness measured for the highest-density foam (70% larger than initial loading stiffness) indicates that the coefficient C_1 is not as small as suggested by the initial loading data.

4.3. Tension–compression asymmetry

Interpretation of the coefficient C_2 is rendered difficult in the case of Vit106 (and other amorphous metals) due to ambiguity in the definition of the ‘solid yield strength’ $\sigma_{y,s}$ used to normalize foam strength data. Equating this factor to the compressive strength of Vit106 (1800 MPa) gave the best-fit value $C_2 = 0.20$, while use of the tensile strength (1200 MPa) gave a higher value of $C_2 = 0.31$. While the latter is comparable to the accepted value for other low-density, open-cell metallic foams, the former suggests a significant additional ‘knockdown’ and would place Vit106 foams nearer the bottom of the empirical range for C_2 [14]. Clarification regarding the definition of $\sigma_{y,s}$ is needed to determine ideal or optimal foam strength and also, therefore, to assess the efficiency of different architectures.

Such clarification can be made by reexamining the geometrical arguments giving rise to Eq. (2). Using a simple but predictive model architecture, Gibson and Ashby [25,31] show that metallic foam yield stress is directly related to the fully plastic moment M_p of a characteristic strut within the model. This quantity, representing the maximum bending moment that can be sustained by a beam, is equal to the applied moment that causes full plasticization of the beam cross-section (a condition known as ‘plastic hinging’). For a beam of uniform pre-

scribed cross-section, M_p can be calculated by solving the equations of force and moment equilibrium within a cross-sectional plane of the beam, given the uniaxial constitutive behavior of the beam material [32].

Although methods exist for solving this problem for many beam and loading geometries, the idealizations inherent in foam structure modeling do not justify a full analysis. The problem is typically solved for uniform doubly symmetric struts assuming elastic-perfectly plastic or power-law strain-hardening constitutive relations [20,33]. Since amorphous metals are known to exhibit perfectly plastic behavior in confined loading [7], it suffices for present purposes to compute the proper normalization factor for elastic-perfectly plastic Vit106 struts with uniaxial tensile and compressive yield strengths of magnitude σ_T and σ_C , respectively; though the method is general, a strut of square cross-section (edge length h) is used to demonstrate. One such strut, in the fully plasticized condition, is shown schematically in Fig. 7. The distance between the neutral axis and the midplane of the strut, y_n , in this condition is determined by equilibrium of normal forces in the tensile and compressive regions:

$$F_T - F_C = A_T \cdot \sigma_T - A_C \cdot \sigma_C = 0, \quad (3)$$

where F_T and F_C are the magnitudes of the tensile and compressive forces associated with each region. Introducing the tensile and compressive cross-sectional areas, $A_T = h \cdot (h/2 + y_n)$ and $A_C = h \cdot (h/2 - y_n)$, into Eq. (3) and solving for y_n yields

$$y_n = \left(\frac{h}{2}\right) \left(\frac{\sigma_C - \sigma_T}{\sigma_C + \sigma_T}\right). \quad (4)$$

As expected, $y_n = 0$ when there is no tension–compression asymmetry ($\sigma_C = \sigma_T$).

With the tensile and compressive regions thus delineated, the internal moments exerted on the cross-section by these stress distributions can be calculated by reducing them to point loads, acting through the centroids (at y_T and y_C , respectively) of the corresponding regions, and in opposition to the applied moment. At the point of collapse the internal moments just balance the fully plastic moment M_p :

$$M_p = F_T \cdot y_T + F_C \cdot y_C. \quad (5a)$$

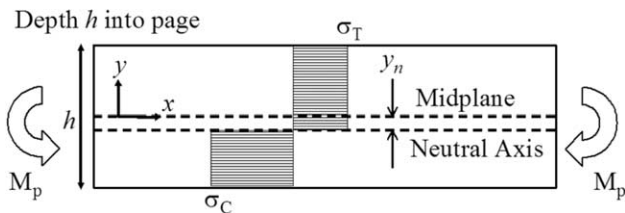


Fig. 7. Schematic illustration of an elastic-perfectly plastic amorphous metal strut (square cross-section of edge length h) in the fully plasticized condition. The distance from the centerline to the neutral axis is given by y_n , and the tensile and compressive strengths are given by σ_T and σ_C , respectively, indicated by the shaded stress distributions.

Introducing Eqs. (3) and (4), as well as $y_T = 1/2(h/2 + y_n)$ and $y_C = 1/2(h/2 - y_n)$ into Eq. (5a) and simplifying provides a compact expression for M_p :

$$M_p = \left(\frac{h^3}{2}\right) \left(\frac{\sigma_C \cdot \sigma_T}{\sigma_C + \sigma_T}\right). \quad (5b)$$

In the absence of tensile/compressive asymmetry, $\sigma_T = \sigma_C = \sigma_y$ and Eq. (5b) simplifies to

$$M_{p0} = \left(\frac{h^3}{4}\right) \cdot \sigma_y. \quad (5c)$$

We retrieve here the relationship used to derive Eq. (2). In the case of tensile/compressive asymmetry, σ_y may be replaced by an effective yield strength $\sigma_{y,\text{eff}}$ in Eq. (5c), so that the conventional form of Eq. (2) may still be used. For a square strut this effective yield stress is found by Eqs. (5b) and (5c):

$$\sigma_{y,\text{eff}} = \frac{2 \cdot \sigma_C \cdot \sigma_T}{\sigma_C + \sigma_T}. \quad (6)$$

Thus, the appropriate strength normalization factor for foams with square struts is the harmonic mean of tensile and compressive strengths, a quantity which always lies closer to the tensile strength, i.e., is below the geometric mean $\sigma_{y,\text{av}} = 1/2(\sigma_T + \sigma_C)$; for Vit106 with $\sigma_T = 1200$ MPa and $\sigma_C = 1800$ MPa [18], the harmonic mean is $\sigma_{y,\text{eff}} = 1440$ MPa, and the geometric mean is $\sigma_{y,\text{av}} = 1500$ MPa. Both square and triangular struts are common and reasonable idealizations for metal foams, and conform to microscopic observations from Vit106 foams. Repeating the analysis for an equilateral triangular strut of equal cross-sectional area gives a more complicated result due to the singly symmetric nature of the cross-section (see Appendix A). The predicted values of effective yield strength depend on the sign of strut curvature (Eqs. (A.4) and (A.5)) but take an average value of 1486 MPa for Vit106, slightly below $\sigma_{y,\text{av}} = 1500$ MPa. Thus, in the absence of detailed knowledge regarding foam architecture, a reasonable approximation is to normalize amorphous metal foam strength data by a geometric mean value of the tensile and compressive yield strengths of the monolithic alloy. In light of the more precise calculations presented here, we use a mean of the effective yield strength for square and triangular struts (1463 MPa), resulting in a best-fit coefficient $C_2 = 0.25$ for the Vit106 foams, within the range reported for crystalline metal foams [14].

4.4. Post-yield and densification behavior

Increasing flow stress in the post-yield linear region (Fig. 3) has been previously observed in crystalline metallic foams, and arises from two primary factors: strain-hardening in deformed struts, and contact forces

developed between nodes connecting these struts [20,34]. Since amorphous metals show perfectly plastic behavior in geometries where plasticity is allowed [7], the first explanation is unlikely to apply to Vit106 foams; the latter, however, is expected to influence flow stresses. Contact forces are likely to develop in the compressed Vit106 foams due to their prominent nodes (Fig. 1(d) and (e)), and increases in reloading stiffness observed at low strains (Fig. 4(b)) further indicate their presence early in the stress–strain curve. It is notable that in pure aluminum foams of similar relative densities and structures, processed by replication of NaCl patterns, steeply rising flow stresses were also observed, and this was confirmed by the aluminum foam studied here [20]. The increases in these aluminum foams were attributed to both intrinsic strain hardening and contact forces.

In this context, the observed increase in relative slope in the post-yield linear region with decreasing Vit106 foam density reflects the fact that yield strength (governed by strut size) decreased more rapidly with density than the contact forces (governed by node size), because of the preferential action of the acid bath on the struts. It may also represent the faster accumulation of damage in the denser samples, as discussed below; the minor pore size dependence corroborates this latter explanation, since the more damage-prone coarse foams showed smaller relative increases in flow stress. The fact that all Vit106 samples showed smaller relative stress increases than the aluminum foam may therefore reflect higher rates of damage in the Vit106.

Densification strain is also known to be sensitive to pore architecture [16]. According to Ashby et al. [14] densification strain is primarily a function of relative density and takes the form

$$\varepsilon_d = (0.9 - 1.0) \cdot \left(1 - 1.4 \left(\frac{\rho}{\rho_s} \right) + 0.4 \left(\frac{\rho}{\rho_s} \right)^3 \right). \quad (7)$$

Another equation is proposed by Chan and Lie [16]:

$$\varepsilon_d = 1 - \alpha \cdot \left(\frac{\rho}{\rho_s} \right)^{1/2}, \quad (8)$$

where α is a constant with a best-fit value $\alpha = 0.85$ for the present Vit106 foams. For the range of densities investigated here, densification strains predicted by Eqs. (7) and (8) are 62–80% and 55–68%, respectively. Both models give acceptable fits to the data (which ranges between 60% and 66%), though Eq. (7) generally slightly overestimates densification strains for Vit106 foam. It is, however, emphasized that the numerical value of densification strain is sensitive to the particular procedure used to calculate it; thus a comparison of this sort is valuable less for its numerical accuracy as for demonstrating that final densification occurs approximately at the same strains in Vit106 foams as in conventional ductile metal foams. This was additionally confirmed by using the

same procedure on the highly ductile pure aluminum foam of comparable relative density, and achieving a value of 61%, within the range measured for Vit106 foams, and between the predictions of Eqs. (7) and (8).

4.5. Energy absorption

Absorption or dissipation of mechanical energy through large strain accumulation at low and relatively constant stress is one of the most unique and important properties of foam materials, making them well suited for packaging and other energy management applications [14]. While there are many ways of quantifying energy absorption capacity, depending on application requirements (e.g., maximum stress transfer or deflection, or minimum foam volume or weight), calculation of strain energy density (per unit volume or mass) dissipated up to densification, as a function of flow stress at 25% strain, allows direct comparison with aluminum foam data compiled by Ashby et al. [14]. As shown in Fig. 8, values of energy density up to densification were in the range of 16–44 MJ/m³ or 16–28 MJ/Mg for Vit106 foams studied here, as compared to 3–20 MJ/m³ and 6–30 MJ/Mg for aluminum foams of the same flow stress range, represented in the shaded region approximately representing the aluminum foam data compiled by Ashby et al. [14]. Therefore, as compared to aluminum foams, Vit106 foams absorbed considerably more

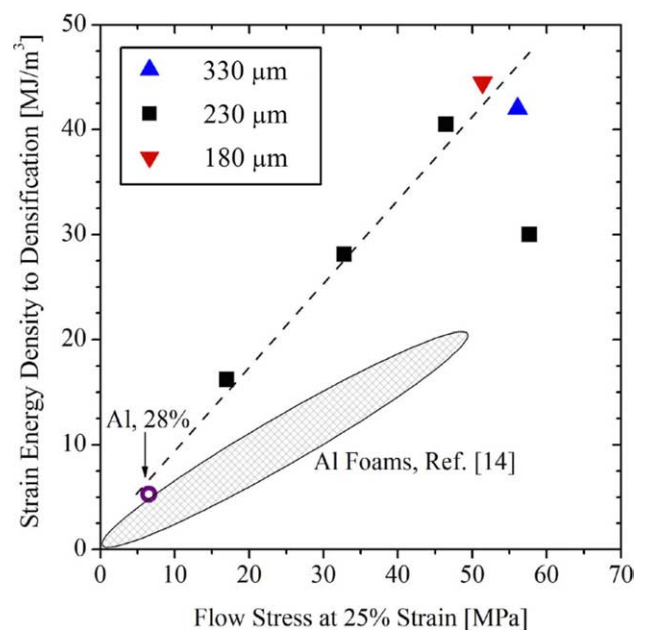


Fig. 8. Strain energy absorbed by Vit106 foams up to densification, per unit foam volume, as a function of flow stress at a nominal strain of 25%. The densest sample (28%) carried high stress but exhibited lower energy absorption than expected due to premature failure. Shown for comparison are the aluminum foam produced by replication of NaCl (open circle) and the approximate range for other aluminum foams, as compiled in Ref. [14]. The dashed line is provided as a visual guide to represent the trend in Vit106 data.

energy per unit volume, but due to higher density, only moderately more energy per unit mass. It is notable that strain energy scales essentially, but not perfectly, linearly with relative density, on account of the varying post-yield slopes, and has no apparent dependence on pore size, despite the substantial differences in serration activity.

Although comparisons of this form are accurate, it should be remembered that high energy absorption in Vit106 foams was partly achieved through large flow stress increases past 25% strain, while many aluminum foams have smaller increases, which are often preferred in energy absorption applications to minimize stress transfer [14]. The replicated aluminum foam tested here offered a more direct comparison, since its structure and behavior closely resembled those of Vit106 foams; indeed, this foam showed an even larger relative flow stress increase than the Vit106 foams, rendering its strain energy density subject to the same increase due to high stresses beyond 25% strain. The energy absorption of this foam was 5 MJ/m^3 (7 MJ/Mg), substantially below that of any Vit106 foam, but close to the value that would be expected from a Vit106 foam of equal flow stress (Fig. 8). Due to the coincidence of the Vit106 trend with the aluminum foam envelope at low stresses, however, this is perhaps fortuitous.

4.6. Damage evolution

The existence of significant internal damage accumulation in the Vit106 foams was evidenced by the pronounced serrations in the stress–strain curves and the simultaneous generation of sparks caused by strut fracture. Given the small number of significant serrations in the foam stress–strain curves (ranging from 12 to 66) relative to the number of struts or nodes per sample (estimated to be on the order of 10^4 for a typical sample), visible serrations represented only the most energetic fractures, most likely of small groups of struts and nodes whose sizes, shapes or orientation relative to the load did not permit ductile deformation by stable shear band formation in bending.

Since flow stress within these serrations was lower than would be expected based on smooth and continuous extrapolation of the stress–strain curve, the actual foams absorbed a smaller amount of strain energy than would hypothetical foams with identical flow characteristics except lacking the brittle failures responsible for serrations. This energy loss was calculated for each serration, using the difference in strain energy density between the actual serrated curve and a curve showing a linear flow stress change over the same strain range, and is a damage parameter capturing both the magnitude of the instantaneous stress drop (itself corresponding to irreversible strain in the foam due to damage) and the strain increment over which the foam recovers the

original flow stress preceding the serration. This damage parameter is shown in Fig. 9 as a cumulative function of macroscopic sample strain. In the interest of avoiding natural statistical fluctuations due to equipment noise and the stochastic nature of the foams, only those serrations occurring after yield (the lowest elastic loads were subject to load cell noise, giving spurious results) and involving instantaneous loss of at least 5% of the flow stress were considered. No such serrations were observed in the aluminum foam.

As shown in Fig. 9, total strain energy lost due to foam damage increased with both relative density (with the exception of the densest sample, for which data extend only to 50% strain due to sample failure) and pore size, indicating that the fewest brittle features were present in low-density foams with fine porosity. This can be understood in terms of foam structure and the unique size effect that governs ductility in amorphous metal struts, an effect that is absent in crystalline metal struts. In these foams, decreased relative density at constant pore size was achieved by thinning of struts at near-constant length; this should clearly improve ductility in Vit106 struts by making them more prone to ductile bending and buckling modes, by improving failure strains in those that already deform in this fashion, and possibly by increasing (for example, in a foam with tapered struts) the proportion of each strut having high

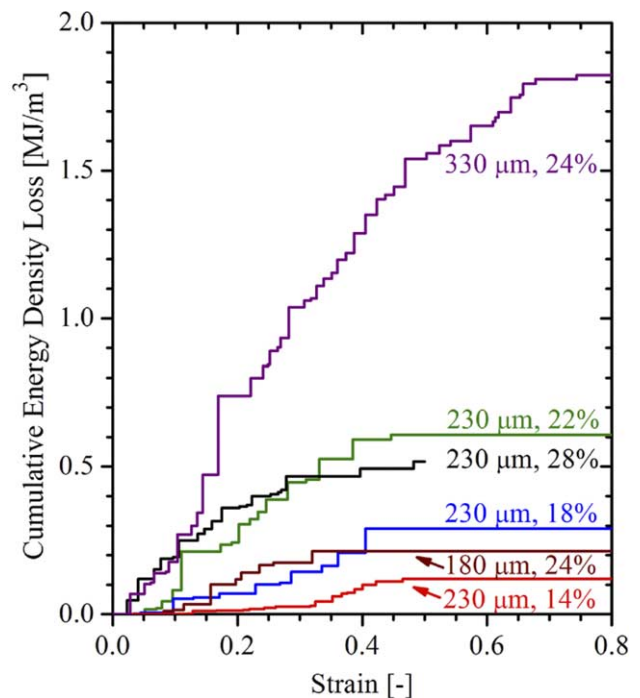


Fig. 9. Cumulative strain energy density lost during recovery from brittle fractures (serrations) during compression as a function of foam strain. Strain energy density loss is estimated by subtracting the actual strain energy density during each serration from that of an idealized stress strain curve lacking serrations and having a linear change in flow stress over the same range.

bending ductility. A similar size effect led to changes in serration activity with pore size; for a given strut shape and arrangement (i.e., a given relative density), decreased absolute dimensions associated with decreased pore size result in higher ultimate bending strains for struts, and thus in reduced serration number and severity. As illustrated in Fig. 2(d)–(g), however, brittle strut failures will always be present, even if all internal features of the foam are well below the ductile limit, given by the thickness at which a bent wire or foil fractures with surface strain equal to the uniaxial failure strain (ca. 1 mm for Vit106 [6]). Indeed, the stochastic nature of the foam structure assures that some small and slender struts will nonetheless fail without plasticity simply due to unfavorable local loading geometry. The total strain energy lost during serration recovery was, however, only a small fraction (0.5–4.3%) of the total strain energy absorption for any given sample.

All curves in Fig. 9 were sublinear, indicating a decaying rate of internal damage with increasing deformation. This was caused by decreasing numbers of serrations at high strain, which in turn resulted from two sources: (1) increasing confinement during densification, preventing unstable fracture in certain struts and nodes; and (2) a ‘weakest link’ damage process in which the least energetic fractures (more numerous due to small average feature sizes) occurred first, followed by more energetic fracture of the smaller population of larger, stronger features whose higher fracture strengths required more severe deformation in order to develop locally. The latter interpretation is supported, generally, by net increases in the energy associated with individual serrations with increasing strain; the scatter in these individual serration energies is too high for a conclusive statement, however, especially in light of the small numbers of serrations present in some of the curves.

Internal damage due to brittle fracture should also be manifest as decreasing stiffness during plastic deformation, as shown in Fig. 4(b) (prior to the increases at high strains resulting from contact forces). Data from comparable aluminum-based foams made by NaCl replication also showed decreasing stiffness after yield [17,20]. Minimum stiffness was 90–95% of the initial stiffness in pure aluminum foam and 70–75% in brittle Al–Si foam, the latter being similar to the measured minimum in Vit106 foam. However, these minima were achieved at much higher sample strains (>15%) in aluminum and Al–Si foams as compared to Vit106 foams (5–7%), perhaps due to the earlier onset of densification in the latter, as discussed above. Thus the ‘damage parameter’ for the Vit106 foam, defined as $\alpha = -(dE/E_0)/d\varepsilon$ with E_0 the initial stiffness (in this case we take E_0 to be the stiffness just prior to yield) and ε the applied macroscopic strain, was $\alpha \sim 9$ for Vit106 foam, as compared to $\alpha < 1$ in pure aluminum and $\alpha \sim 2$ in Al–Si foams [17]. The rate of strut failure and internal damage was conse-

quently much higher in Vit106 foams than in comparable Al-based foams, even those considered brittle by aluminum standards. In light of this fact, it is remarkable that compressive strains in the vicinity of 80% were sustained by all but one of the Vit106 foams tested.

5. Conclusions

Compressive mechanical properties of low-density, open-cell Zr-based amorphous metal foams were measured for relative densities in the range of 14–28% and pore sizes of 150–355 μm . Results documented here provide further support for the existence of large compressive ductility (in the vicinity of 80%) arising from extensive plastic strut bending. Models developed for conventional metallic foams were found to adequately predict strength and stiffness in the amorphous metal foams, especially after appropriate modifications were made reflecting the tension–compression asymmetry of amorphous metals. Deviation from the models was apparent, however, in the lowest density foam, as a result of processing-related thinning of struts.

Brittle fracture of a small number of struts within the macroscopically ductile foams resulted in internal damage, assessed through stiffness evolution. The most energetic of these fracture events were visible as serrations on the stress–strain curves, and the cumulative damage associated with these serrations increased with both foam density and pore size. Internal damage accumulated more rapidly in Vit106 foam than in comparable aluminum foams, but did not alter the ability of Vit106 foams to sustain very high macroscopic compressive strains in the vicinity of 80% as compared to bulk Vit106 ($\sim 2\%$), with associated high strain energy densities of 16–44 MJ/m^3 , and did not produce an inverse dependence of strength on pore size, as in brittle ceramic foams.

With further optimization, amorphous metal foams could represent promising alternatives to conventional metallic foams in a range of applications requiring high ductility together with the high strength, wear/corrosion resistance, and good processability associated with amorphous metals, e.g., lightweight structures, energy management, and biomaterials.

Acknowledgments

The authors acknowledge the financial support of the DARPA Structural Amorphous Metals Program (ARO Contract No. DAAD 19-01-1-0525) and thank the Caltech Center for Structural Amorphous Metals for providing supplies and facilities to arc-melt Vit106 buttons. The authors also thank Dr. C. San Marchi (currently at Sandia National Laboratories, Livermore)

for his assistance at the early stages of this project and for fabrication of the aluminum foam sample tested in compression.

Appendix A. Derivation of effective yield stress for struts with triangular cross-section

Evaluation of the fully plastic moment of a strut having uniform equilateral triangular cross-section (with edge length a) proceeds under the same assumptions and with the same approach as outlined in the text for square cross-sections. For simplicity, the triangular strut is assumed to bend in a plane intersecting one of its edges along the entire length of the beam, and passing through the midpoint of the opposing face (i.e., a vertically oriented plane extending perpendicularly to the cross-section in Fig. A.1). Depending on the sign of the applied moment, one of the two cases represented in Fig. A.1 applies. For the case represented in Fig. A.1(a), the area of the tensile region is $A_T = z^2/\sqrt{3}$. The area of the compressive region is $A_C = \sqrt{3}(a^2/4 - z^2/3)$, found as the difference between A_T and the total strut area $A_{tot} = \sqrt{3}a^2/4$. Introducing these quantities into the force balance equation, Eq. (3), and solving for z locates the plastic neutral axis

$$z = \frac{a}{2} \cdot \left(\frac{3\sigma_C}{\sigma_T + \sigma_C} \right)^{1/2}, \tag{A.1}$$

where σ_T and σ_C are the magnitudes of the tensile and compressive strengths, as in the main text. The centroid of the tensile region lies at a distance equal to one-third the height of the triangle above its base, or $y_T = z/3$. The centroid of the isosceles trapezoidal compressive region lies at a distance $(h/3) \cdot (2a' + b')/(a' + b')$ above the bottom edge of the strut, where h , a' , and b' are the height, upper, and lower base of the trapezoidal region, respectively (Fig. A.1(a)). Noting that this bottom edge is at a distance $a\sqrt{3}/2 - z$ from the neutral axis, the distance from the neutral axis to the centroid of the compressive region is found to be

$$y_C = \frac{3a^2 - 2z^2 - \sqrt{3}az}{6z + 3\sqrt{3}a}. \tag{A.2}$$

Introducing the distances y_T and y_C , the areas A_T and A_C and Eq. (A1) into the moment balance equation (Eq. (5a)) and solving for M_p gives the fully plastic moment of the beam under the assumed loading conditions

$$M_p = \left(\frac{a^3}{4} \right) \left(\frac{\sigma_C \cdot \sigma_T}{\sigma_C + \sigma_T + \sqrt{\sigma_C(\sigma_C + \sigma_T)}} \right). \tag{A.3a}$$

Since the area of a triangular strut of edge length a is not equal to the area of a rectangular strut of edge length a , a foam composed of such struts need not be of the same relative density as the foam represented by

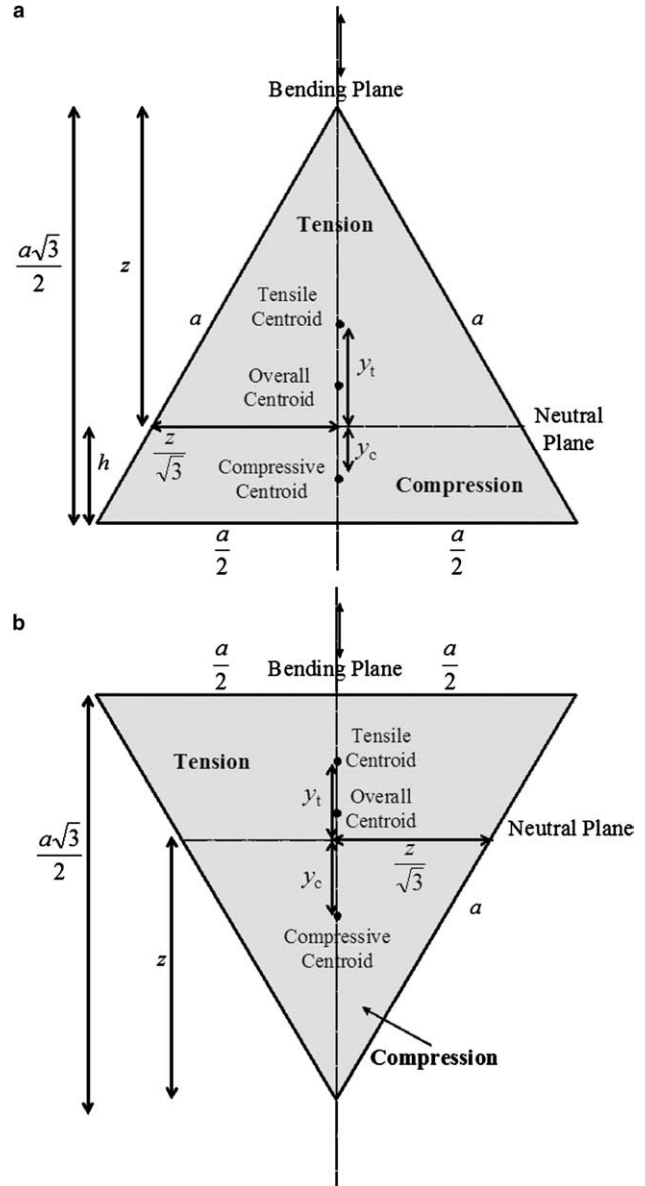


Fig. A.1. Schematic cross-sectional view of a strut of equilateral triangular shape, subjected to bending in a plane oriented perpendicularly to the page. In (a) the applied moment produces tension along the edge of the strut and compression along the opposing face; in (b) it has the opposite sense, producing compression along the edge and tension in the face.

the rectangular strut of Fig. 7. Thus we calculate the effective edge length h_{eff} of a rectangular strut with equal cross-sectional area to the strut in Fig. A.1(a), by equating their respective areas, with the result that $h_{eff} = 3^{1/4} \cdot a/2$. Expressing Eq. (A.3a) in terms of this quantity gives

$$M_p = \left(\frac{h_{eff}^3}{4} \right) \left(\frac{8}{3^{3/4}} \right) \left(\frac{\sigma_C \cdot \sigma_T}{\sigma_C + \sigma_T + \sqrt{\sigma_C(\sigma_C + \sigma_T)}} \right). \tag{A.3b}$$

Equating Eqs. (A.3b) and (5b) provides the effective yield stress

$$\sigma_{y,\text{eff}} = \left(\frac{8}{3^{3/4}}\right) \left(\frac{\sigma_C \cdot \sigma_T}{\sigma_C + \sigma_T + \sqrt{\sigma_C(\sigma_C + \sigma_T)}}\right). \quad (\text{A.4})$$

Performing the same analysis for an oppositely oriented applied moment (Fig. A.1(b)) gives a similar result

$$\sigma_{y,\text{eff}} = \left(\frac{8}{3^{3/4}}\right) \left(\frac{\sigma_C \cdot \sigma_T}{\sigma_C + \sigma_T + \sqrt{\sigma_T(\sigma_C + \sigma_T)}}\right). \quad (\text{A.5})$$

Using $\sigma_T = 1200$ MPa and $\sigma_C = 1800$ MPa [18] for Vit106, Eqs. (A.4) and (A.5) provide values $\sigma_{y,\text{eff}} = 1424$ MPa and $\sigma_{y,\text{eff}} = 1548$ MPa, respectively. Since both loading configurations are equally likely for any given strut within a foam, we take the effective yield stress of a triangular beam to be the mean of these quantities, 1486 MPa.

References

- [1] Loffler JF. *Intermetallics* 2003;11:529.
- [2] Wang WH, Dong C, Shek CH. *Mater Sci Eng* 2004;R44:45.
- [3] Schroers J, Johnson WL. *Phys Rev Lett* 2004;93.
- [4] Wada T, Inoue A. *Mater Trans* 2004;45:2761.
- [5] Brothers AH, Dunand DC. *Adv Mater* 2005;17:484.
- [6] Conner RD, Johnson WL, Paton NE, Nix WD. *J Appl Phys* 2003;94:904.
- [7] Conner RD, Li Y, Nix WD, Johnson WL. *Acta Mater* 2004;52:2429.
- [8] Brothers AH, Dunand DC. *Scripta Mater* 2005 (in press).
- [9] Schroers J, Veazey C, Johnson WL. *Appl Phys Lett* 2003;82:370.
- [10] Wada T, Inoue A. *Mater Trans* 2003;44:2228.
- [11] Brothers AH, Dunand DC. *Appl Phys Lett* 2004;84:1108.
- [12] Schroers J, Veazey C, Demetriou MD, Johnson WL. *J Appl Phys* 2004;96:7723.
- [13] Brothers AH, Scheunemann R, DeFouw JD, Dunand DC. *Scripta Mater* 2005;52:335.
- [14] Ashby MF, Evans AG, Fleck NA, Gibson LJ, Hutchinson JW, Wadley HNG. *Metal Foams: A Design Guide*. Boston (MA): Butterworth–Heinemann; 2000.
- [15] Ross SM. *Introduction to Probability and Statistics for Engineers and Scientists*. New York (NY): Wiley; 1987.
- [16] Chan KC, Xie LS. *Scripta Mater* 2003;48:1147.
- [17] San Marchi C, Despois JF, Mortensen A. *Acta Mater* 2004;52:2895.
- [18] Choi-Yim H, Conner RD, Szuecs F, Johnson WL. *Acta Mater* 2002;50:2737.
- [19] San Marchi C, Mortensen A. In: Degischer HP, Kriszt B, editors. *Handbook of Cellular Metals: Production, Processing, Applications*. Weinheim: Wiley–VCH; 2002 [chapter 2].
- [20] San Marchi C, Mortensen A. *Acta Mater* 2001;49:3959.
- [21] Gaillard C, Despois JF, Mortensen A. *Mater Sci Eng A* 2004;374:250.
- [22] Nieh TG, Higashi K, Wadsworth J. *Mater Sci Eng A* 2000;283:105.
- [23] Simone AE, Gibson LJ. *Acta Mater* 1998;46:2139.
- [24] Choi-Yim H, Busch R, Koster U, Johnson WL. *Acta Mater* 1999;47:2455.
- [25] Gibson LJ, Ashby MF. *Cellular Solids: Structure and Properties*. 2nd ed. Cambridge (MA): Cambridge University Press; 1997.
- [26] Brezny R, Green DJ. *Acta Metall Mater* 1990;38:2517.
- [27] Wen CE, Yamada Y, Shimojima K, Chino Y, Hosokawa H, Mabuchi M. *Mater Lett* 2004;58:357.
- [28] Morgan JS, Wood JL, Bradt RC. *Mater Sci Eng* 1981;47:37.
- [29] Huang JS, Gibson LJ. *J Mater Sci Lett* 1993;12:602.
- [30] Despois JF, Conde Y, San Marchi C, Mortensen A. *Adv Eng Mater* 2004;6:444.
- [31] Gibson LJ, Ashby MF. *Proc Roy Soc Lond A Mater* 1982;382:43.
- [32] Jirásek M, Bazant ZP. *Inelastic Analysis of Structures*. Chichester (UK): Wiley; 2002.
- [33] Gibson LJ. *Annu Rev Mater Sci* 2000;30:191.
- [34] Kenesei P, Kadar C, Rajkovits Z, Lendvai J. *Scripta Mater* 2004;50:295.